[1.]Ştefan ŢĂLU, [2,3,4.]Kipkurui RONOH, [2,3,5.]Dinara SOBOLA

EFFECT OF ULTRAFAST LASER ABLATION ON THE SURFACE TOPOGRAPHY OF MONEL® ALLOY 400

[1.] Technical University of Cluj–Napoca, The Directorate of Research, Development and Innovation Management (DMCDI), Cluj–Napoca, ROMANIA
[2.] Brno University of Technology, Central European Institute of Technology, Brno, CZECH REPUBLIC.
[3.] Brno University of Technology, Faculty of Electrical Engineering and Communication, Department of Physics, Brno, CZECH REPUBLIC.
[4.] Dedan Kimathi University of Technology, Department of Mechanical Engineering, Nyeri, KENYA
[5.] Czech Academy of Sciences, Institute of Physics of Materials, Brno, CZECH REPUBLIC

Abstract: This study examines the influence of ultrafast laser ablation on the surface morphology of Monel® alloy 400, a nickel–copper alloy known for its corrosion resistance and high durability in marine environments. Monel® 400 is extensively used in the production of marine components where surface characteristics play a critical role in their performance and longevity. To investigate the effects of laser ablation, polished Monel® 400 samples were exposed to ultrafast laser pulses under varying fluence levels and operational parameters. The ablation process generated distinct surface features, including the formation of well–defined square cavities. These features were thoroughly characterized using profilometry to measure alterations in surface roughness, texture, and topography. The findings demonstrate how laser parameters influence the material's microstructure and surface profile, offering potential strategies for tailoring the surface properties of Monel® 400 for specific marine applications. Furthermore, the study underscores the role of ultrafast laser processing as a precise tool for surface engineering, with implications for improving the wear resistance, corrosion behavior, and overall functionality of Monel® alloy components in harsh operating environments.
Keywords: Laser treatment, marine equipment components, MONEL® alloy 400, surface topography

1. INTRODUCTION

Nickel–based alloys are extensively utilized in marine engineering applications due to their exceptional mechanical strength, oxidation resistance, and superior corrosion resistance, particularly in harsh environments with high salinity, such as seawater [1]. These alloys, with nickel as the primary component, are typically combined with elements like chromium, copper, molybdenum, and iron to enhance specific properties, such as high–temperature strength and improved corrosion resistance [2]. Monel® alloy 400, a single–phase nickel–copper alloy, contains approximately 62–68% nickel and 28–34% copper, along with trace amounts of iron, manganese, carbon, sulfur, and silicon [3]. This composition affords Monel® 400 remarkable resistance to corrosive media, such as seawater and high–temperature steam, making it a preferred material for various marine applications [4–6].

Monel® alloy 400's versatility arises from its solid–solution strengthening mechanism, enabling it to be hardened exclusively by cold working [6,7]. The alloy's resistance to corrosion in rapidly flowing seawater, along with its resistance to stress–corrosion cracking in freshwater, makes it ideal for marine engineering. The alloy exhibits excellent mechanical properties across a broad temperature range, from sub–zero temperatures to 550 °C, which broadens its application scope. However, its performance is limited in oxidizing environments, such as nitric acid, due to the high copper content [2,8–10].

Monel® 400 finds widespread application in the fabrication of marine components like evaporators, valves, pumps, heat exchangers, and diffusers [3]. Beyond the marine sector, it is employed in chemical processing industries and desalination plants due to its ability to withstand chloride–rich environments and corrosive solutions [9,11].

The advent of laser processing has revolutionized material modification techniques, offering precision and speed in altering surface properties. Ultrafast lasers, particularly femtosecond (fs) and picosecond (ps) lasers, have emerged as powerful tools for micro–processing materials [12,13]. These lasers, which emit extremely short bursts of energy, are distinguished by their ability to deliver high peak power in very short time intervals, leading to precise material ablation with minimal thermal effects [14]. Femtosecond (fs) and picosecond (ps) laser ablation is now a critical technique in both scientific and industrial fields, allowing precise control over surface modifications while maintaining material integrity. The combination of high peak power and very short interaction time ensures that the laser energy is deposited quickly into the material [15]. Due to the short interaction time (10^{-12} s for ps lasers), heat–affected zones (HAZ) are minimized, reducing the risk of cracks, material resolidification, or other defects that typically arise during traditional laser processing methods [7,16]. Although extensive studies have

ISSN 1584 – 2665 (printed version); ISSN 2601 – 2332 (online); ISSN-L 1584 – 2665

explored the application of ultrafast lasers in processing various metals and alloys, research on their application to Monel® alloy 400 remains scarce [7,10, 11, 17]. The relationship between laser processing parameters, such as fluence, and the resulting surface morphology on Monel® 400 has yet to be comprehensively studied. This gap in knowledge is critical because surface topography in engineering components is paramount to their functionality, durability, and aesthetic quality.

The three–dimensional (3D) surface topography of a material, including its texture, peaks, valleys, and overall geometry, directly influences how it interacts with its environment, affecting properties such as adhesion, wear, corrosion resistance, and overall performance in service [18–22]. Surface morphology, defined by features such as roughness, texture, and microstructural characteristics, is essential for assessing how materials behave under operational conditions [23–27]. Advanced surface characterization techniques, such as profilometry, scanning electron microscopy, and atomic force microscopy, enable detailed quantification of these surface features and offer valuable insights into surface performance and the distribution of micro– and nanostructures. Such insights are particularly relevant in fields such as tribology, where surface interactions influence friction, wear, and lubrication, and in material science, where surface modifications can enhance the properties of engineering materials [28–32]. Conversely, standards such as ISO 25178–2:2012 offer a comprehensive framework for analyzing 3D surface roughness and texture parameters.

In this study, the influence of ultrafast laser ablation on the surface topography of Monel® alloy 400 was investigated.

2. EXPERIMENTAL DETAILS

The research material was a clean, polished, commercially available Monel® alloy 400 with 10 ×10 × 1 mm dimensions. The alloy was subjected to fine grinding (with SiC foils of # 2000) and polishing (with 1 µm abrasive diamond suspensions). The polished sample was ultrasonically washed with acetone and ethanol and dried with pressurized air to remove surface impurities. The aim of obtaining a mirror–like surface finish is to ensure that the laser irradiation is uniformly distributed on the surface. Table 1 provides the percentage weight composition of the elements on Monel® alloy 400.

Table 1. Elemental composition of the Monel® alloy 400. (wt.%).

Ni	Cu	Fe	Mn	Si	C	S
Remainder	28 – 34	2.5	2	0.5	0.3	0.024

The ablation of the alloy was carried out using a picosecond laser system (Perla®100, Hilase, Dolní Břežany, Czech Republic [15]. The experimental setup of the system is shown in Fig. 1. This laser type is specialized for the microprocessing of materials. The laser system produced beams in Gaussian shape mode. The linearly polarised laser beams were focussed onto the surface of the alloy in a perpendicular direction using a focusing lens. The material was held on an X–Y table, and the laser scanning was carried out using a scanning head (intelliSCAN 14, Scanlab, Puchheim, Germany) in bidirectional scan lines.

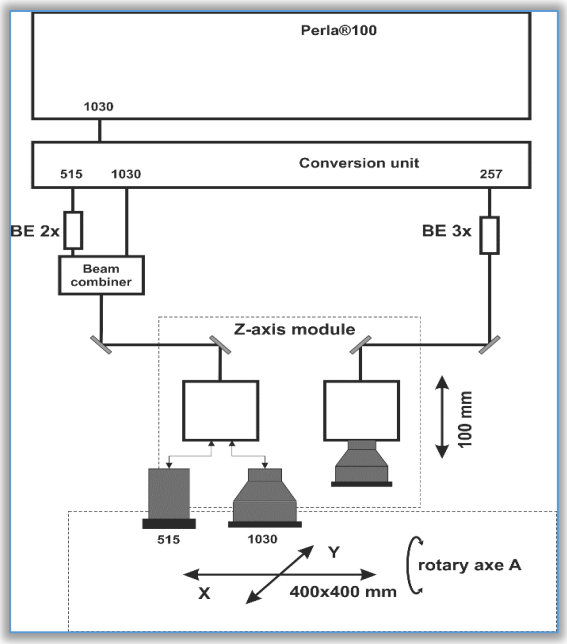

Figure 1. Schematic diagram of the experimental set–up of the Perla® 100 ps laser

Characteristics of the Perla®100 ps laser were: average laser power = 60 W; maximum peak energy = 1 mJ; frequency = 60 kHz; pulse duration = 1 ps; wavelength = 1030 nm; focused spot diameter D = 25 µm at $1/e^2$ value; focal length = 100 mm; beam quality factor, $M^2 \leq 1.3$.

Raster scanning was carried out following an ablation pattern drawn by Direct Machining Control (DMC) 1.7.60 (64bit) software (Direct Machining Control, UAB Vilnius, Lithuania). The cross–hatching patterning at ablation directions of 90°/–90° was used for ablation, where the sample was ablated with the first plane direction being 90°, while the

ISSN 1584 – 2665 (printed version); ISSN 2601 – 2332 (online); ISSN-L 1584 – 2665

second plane direction was −90°. In laser ablation, the selection of cross–hatching scanning patterns ensures uniformity of material removal in various directions and facilitating the management of thermal effects by distributing heat more evenly. The ablation was conducted in ambient conditions. The laser fluence, L, used in the laser ablation varied for each sample:

a. 1 J/cm^2 (sample S1);
b. 4 J/cm^2 (sample S2);
c. 8 J/cm^2 (sample S3), and
d. 15 J/cm^2 (sample S4).

The laser beam was scanned on the surfaces of the samples at a scanning velocity, V of 100 mm/s, with a hatching distance H of 5 µm, and one scanning pass. The sample's surface area subjected to laser ablation was 2.0 x 2.0 mm². After laser ablation, the samples were cleaned ultrasonically using ethanol and dried by pressurized air. The focussed diameter D was used for all calculations involved [1]. The laser pulse overlap (PO) was 93 %, while the scanning line overlap (LO) was 80 % and was applicable for laser ablation [7,13]. The samples were fully ablated with PO of 93 % and LO of 80 % to create square cavities.

Following laser ablation, the surfaces of the samples were subjected to characterization. The surface roughness of the ablated surfaces of the samples was measured by a mechanical profilometer (Dektak XT, Bruker, Billerica, MA, USA). The ablated samples were placed on an automatic X–Y stage with a vertical range of 56 mm. The equipment has a vertical and lateral resolution of up to 0.1 nm and 0.5 µm, respectively. The measuring tip of the profilometer used had a radius of 2 µm. A surface area of 300 × 300 µm^2 was analysed, and the duration of 10 µs per point was utilised for good resolution. The measurements were performed in a cleanroom class 1000, where the temperatures were controlled to 24 °C. The surface morphology was analyzed using MountainsMap Premium Software ver 10 [34].

3. RESULTS AND DISCUSSION

2–D profilometer images of analyzed samples scanned over 300 × 300 µm² surface area are shown in Fig. 2, a–d.

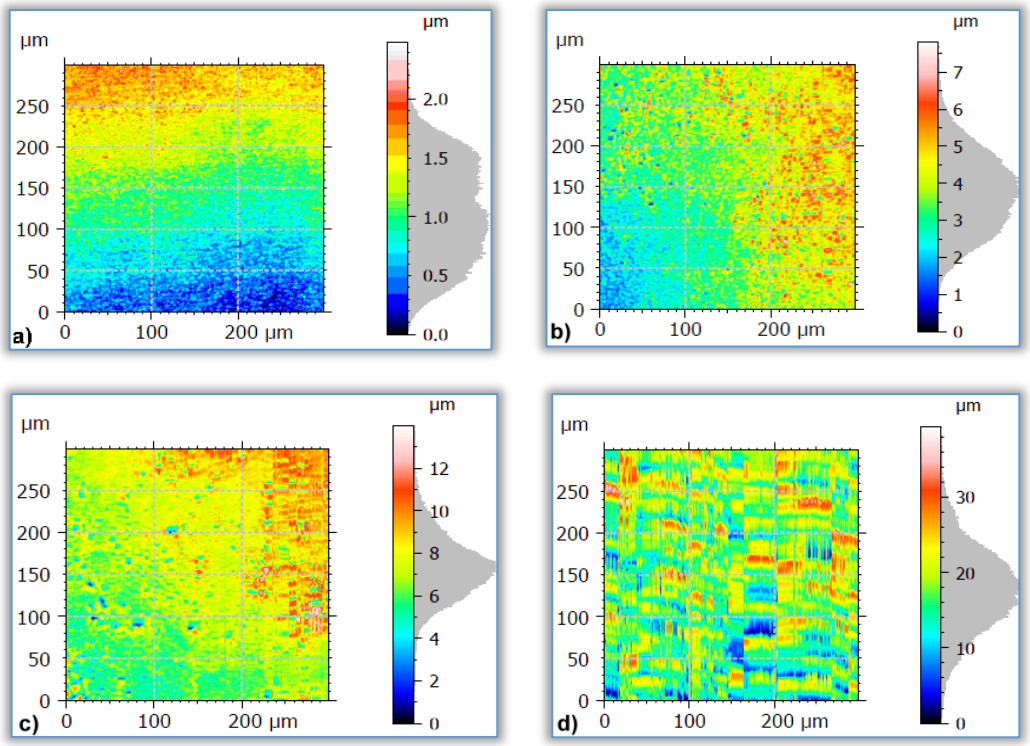

Figure 2. 2–D profilometer images of analyzed samples: a) S1, b) S2, c) S3, and d) S4.

The 2–D profilometer images of the analyzed samples – labeled as S1, S2, S3, and S4 – offer a detailed visualization of the surface topography and roughness. Each image corresponds to a distinct sample, providing insight into its surface characteristics, with its unique roughness features and height variations.

ISSN 1584 – 2665 (printed version); ISSN 2601 – 2332 (online); ISSN-L 1584 – 2665

The Abbott–Firestone curves are essential for characterizing the surface topography of materials. In this study, these curves were derived from profilometry data obtained by scanning the surface of the analyzed samples over a 300 × 300 μm² area. The curves, shown in Fig. 3 (a–d), provide a deeper understanding of the distribution of surface heights and their potential implications for functional properties. Also, the Abbott–Firestone curve provides insight into the load–bearing capacity of a surface. By analyzing the proportion of surface material at different heights, one can predict how the material will behave under mechanical stress. A steep curve in certain regions indicates a high density of peaks or valleys, which can affect how the material interacts with other surfaces, impacting friction, wear, or coating adherence. A surface with a larger portion of material above the median line of the curve may have better wear resistance since more material is available to bear the load before the surface wears down. Conversely, surfaces with deeper valleys (shown in the upper regions of the curve) might indicate areas prone to early wear or failure. The values corresponding for the texture directions parameters of analyzed samples are given in Table 2.

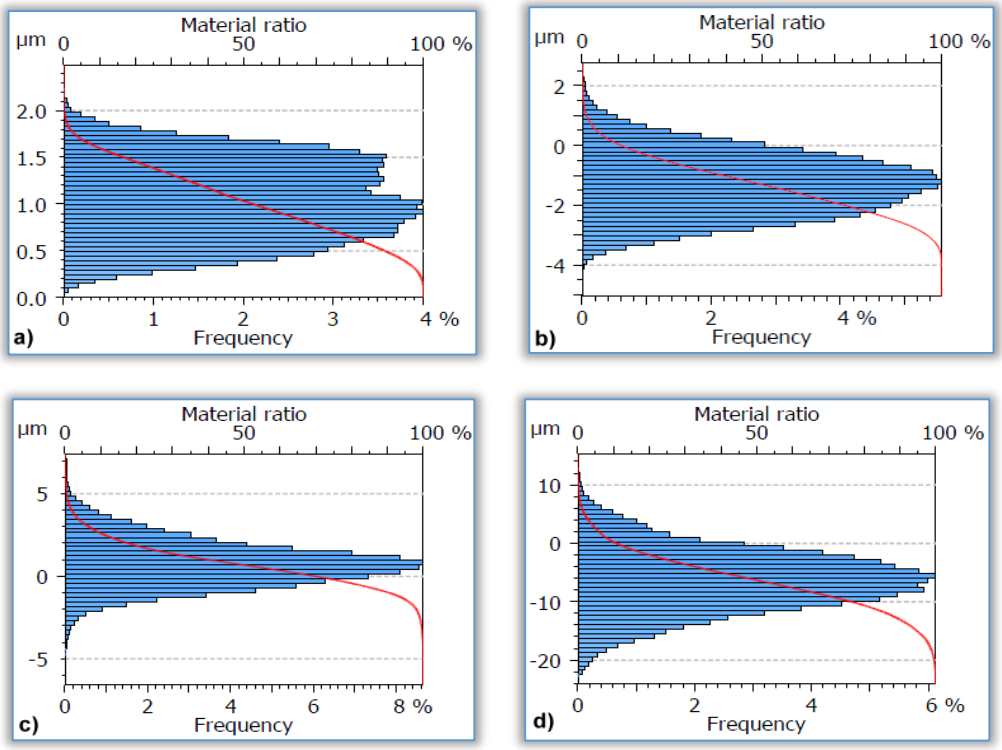

Fig. 3. The Abbott–Firestone curves of analyzed samples: a) S1, b) S2, c) S3, and d) S4.

Table 2. The texture directions parameters of the analyzed samples

Parameters	Unit	Sample S1	Sample S2	Sample S3	Sample S4
First direction	[°]	0.0094	89.97	89.98	90.01
Second direction	[°]	44.98	180.0	180.0	95.17
Third direction	[°]	90.03	44.97	116.5	83.02

The angular values for the first direction in the table 2 are notably distinct across the samples.
For sample S1, the first direction is close to 0° (0.0094°), indicating that the texture aligns nearly horizontally with the reference axis, suggesting a uniform and well–defined surface texture in this direction. For samples S2, S3, and S4, the first direction values (89.97°, 89.98°, and 90.01°, respectively) are very close to 90°, meaning that the surface features are aligned almost perpendicular to the reference axis. This perpendicular alignment may indicate a highly structured or uniform surface pattern, which could affect frictional properties and how the surface interacts with external forces. For sample S1, the second direction is at 44.98°, suggesting that the secondary surface texture is diagonally oriented relative to the reference axis. This might indicate a more complex surface pattern with intersecting features. For samples S2 and S3, both samples have a second direction of 180.0°, meaning their secondary texture is aligned with the reference axis.

ISSN 1584 – 2665 (printed version); ISSN 2601 – 2332 (online); ISSN-L 1584 – 2665

Such alignment could be the result of directional processing methods, such as sputtering, that induce uniform surface patterns. For sample S4, with a second direction of 95.17°, this sample shows a deviation from the horizontal and vertical alignment, suggesting that the surface has a more intricate and less regular texture in the secondary direction. For sample S1, the third direction at 90.03° aligns with the perpendicular axis, further supporting the idea that this sample has a highly ordered and structured surface texture, possibly from a controlled fabrication process. For sample S2, the third direction is 44.97°, close to the second direction of S1, which indicates that this sample has a more varied surface texture, with multiple intersecting directions of features. For sample S3, a third direction of 116.5° indicates a more complex angular distribution of surface features, which might introduce anisotropy in the material's performance, particularly in mechanical or optical applications. For sample S4, with an angle of 83.02°, this value is near perpendicular but slightly off, indicating that the tertiary features deviate from perfect alignment, adding to the complexity of the surface texture. The close–to–90° alignment in samples S2, S3, and S4 suggests high uniformity in one direction, which might enhance directional properties such as friction resistance or mechanical strength. However, this can also lead to vulnerabilities in directions where the surface texture is less defined.

Table 3 provides a comprehensive set of statistical parameters for the analyzed samples, according to the ISO 25178–2:2012 standards [33].

Table 3. The statistical parameters of the samples according with ISO 25178–2: 2012.

The statistical parameters	Symbol	Samples			
		S1	S2	S3	S4
Height Parameters					
Root mean square height	Sq [µm]	0.414	1.028	1.433	5.255
Skewness	Ssk [–]	0.016	0.139	0.317	0.043
Kurtosis	Sku [–]	2.090	2.633	3.820	3.088
Maximum peak height	Sp [µm]	1.440	4.061	6.644	21.59
Maximum pit height	Sv [µm]	1.042	3.749	7.335	17.77
Maximum height	Sz [µm]	2.483	7.810	13.98	39.36
Arithmetic mean height	Sa [µm]	0.350	0.840	1.109	4.165
Functional Parameters					
Areal material ratio	Smr [%]	17.92	0.1814	0.1361	0.0043
Inverse areal material ratio	Smc [µm]	0.5548	1.344	1.863	6.534
Spatial Parameters					
Auto–correlation length	Sal [µm]	92.57	88.34	73.26	10.52
Hybrid Parameters					
Root mean square gradient	Sdq [–]	0.1490	0.6097	0.8615	4.061
Developed interfacial area ratio	Sdr [%]	1.094	15.17	24.87	219.1
Functional Parameters (Volume)					
Material volume	Vm [$\mu m^3/\mu m^2$]	0.01205	0.04697	0.08602	0.2829
Void volume	Vv [$\mu m^3/\mu m^2$]	0.5668	1.391	1.949	6.817
Peak material volume	Vmp [$\mu m^3/\mu m^2$]	0.01205	0.04697	0.08602	0.2829
Core material volume	Vmc [$\mu m^3/\mu m^2$]	0.4217	0.9904	1.232	4.638
Core void volume	Vvc [$\mu m^3/\mu m^2$]	0.5313	1.296	1.805	6.211
Pit void volume	Vvv [$\mu m^3/\mu m^2$]	0.03548	0.09428	0.1439	0.6056
Feature Parameters					
Density of peaks	Spd [$1/\mu m^2$]	0.01966	0.01445	0.0062	0.0070
Arithmetic mean peak curvature	Spc [1/µm]	0.2355	0.5392	1.009	5.376
Ten point height	S10z [µm]	2.216	7.167	13.00	35.63
Five point peak height	S5p [µm]	1.198	3.796	6.581	19.19
Five point pit height	S5v [µm]	1.018	3.371	6.417	16.43
Mean dale area	Sda [μm^2]	101.1	70.63	95.51	117.2
Mean hill area	Sha [μm^2]	46.53	62.40	138.1	116.4
Mean dale volume	Sdv [μm^3]	1.716	6.249	13.27	54.80
Mean hill volume	Shv [μm^3]	1.364	8.290	21.94	90.42

The Root mean square height (Sq) parameter represents the standard deviation of the surface height, providing a measure of surface roughness. The values range from 0.414 µm for S1 (the smoothest surface) to 5.255 µm for S4, indicating a significant increase in roughness for the latter. The larger Sq value for S4 suggests it has the roughest surface, which could affect its wear behavior or optical properties. The Skewness (Ssk) measures the asymmetry of the height distribution. Positive values for all samples indicate that the surfaces have more peaks than valleys. S3, with the highest skewness

ISSN 1584 – 2665 (printed version); ISSN 2601 – 2332 (online); ISSN-L 1584 – 2665

(0.317), has a more pronounced number of peaks compared to the others, which may influence how it interacts with contact surfaces, possibly increasing friction or adhesion.

The Kurtosis (Sku) indicates the sharpness or flatness of the surface texture. For S1 and S2, values near 2 suggest a relatively normal distribution of heights, while S3 and S4, with higher kurtosis values (3.820 and 3.088, respectively), indicate sharper surface features or peaks, which could lead to higher localized stresses during contact or wear. The Maximum peak height (Sp) and Maximum pit height (Sv) parameters represent the maximum vertical deviations (peaks and pits) from the mean plane. S4 has extreme values for both Sp (21.59 μm) and Sv (17.77 μm), demonstrating significant surface irregularities.

The Maximum height (Sz) represents the total height difference between the highest peak and the deepest valley on the surface. S4, with a value of 39.36 μm, shows the greatest overall surface roughness, suggesting it may experience the highest friction or wear in tribological applications, while S1 (2.483 μm) shows a relatively smoother surface.

The arithmetic mean height (Sa) quantifies surface roughness but in terms of the average of the absolute heights. S4's value (4.165 μm) is significantly higher than the others, reaffirming its rough surface compared to the smoother S1 (0.350 μm). S4 shows a very low Areal material ratio (Smr) (0.0043%), indicating a very small proportion of the surface is load–bearing at the reference height, which suggests that the surface has large voids or high peaks. Inverse areal material ratio (Smc), on the other hand, is significantly higher for S4 (6.534 μm), meaning that deeper layers contribute to load–bearing, potentially reflecting a rougher but more porous surface.

The Auto–correlation length (Sal) describes the distance over which surface heights become uncorrelated, essentially a measure of surface texture wavelength. S4, with a significantly smaller Sal (10.52 μm), indicates that its surface texture is more fine–grained and has closely spaced features, in contrast to S1 (92.57 μm), which has a more widely spaced texture. The Root mean square gradient (Sdq) parameter represents the rate of change of the surface height, providing information on the surface's steepness. S4, with the highest Sdq (4.061), has a steep and rugged surface, which could result in higher friction and wear in dynamic applications. The lower value for S1 (0.1490) suggests a much smoother, less steep surface.

The developed interfacial area ratio (Sdr) parameter quantifies the increase in surface area due to surface texture. S4 shows a dramatic increase in surface area (219.1%), indicating a highly developed and rough texture, which can enhance surface interactions such as adhesion or chemical reactions. S1, with the smallest increase (1.094%), has a relatively flat surface, leading to minimal surface area expansion. Material volume (Vm) represents the volume of solid material above a certain reference plane, while Void volume (Vv) represents the volume of voids below that plane. S4, with the highest Vm (0.2829 $\mu m^3/\mu m^2$) and Vv (6.817 $\mu m^3/\mu m^2$), indicates a surface with significant material peaks and deep voids, suggesting that it can hold larger amounts of fluid in voids, potentially useful for lubrication or fluid retention. S1, with much smaller values, represents a more compact and uniform surface.

Core material volume (Vmc) and Core void volume (Vvc) parameters describe the material and void volumes in the core of the surface, which typically carries most of the mechanical load. S4 has much larger core volumes (Vmc = 4.638 $\mu m^3/\mu m^2$, Vvc = 6.211 $\mu m^3/\mu m^2$) compared to S1, reflecting its rougher, more porous structure. Density of peaks (Spd) measures the number of peaks per unit area. S1 has the highest peak density (0.01966 peaks/μm^2), suggesting a more uniform and densely packed surface compared to S4, which has fewer peaks (0.0070 peaks/μm^2), consistent with its larger, more irregular surface features.

Arithmetic mean peak curvature (Spc) parameter quantifies the sharpness of peaks. S4, with the highest value (5.376 1/μm), indicates sharper and more pronounced peaks, which could result in higher localized stress concentrations. S1 has the lowest peak curvature (0.2355 1/μm), suggesting smoother, more rounded peaks. Mean dale area (Sda) and Mean hill area (Sha) parameters quantify the average areas of valleys (dales) and peaks (hills). S4 has the largest dale (117.2 μm^2) and hill (116.4 μm^2) areas, indicating broad and pronounced surface features, while S1 has smaller and more compact dales and hills, correlating with its overall smoother texture.

ISSN 1584 – 2665 (printed version); ISSN 2601 – 2332 (online); ISSN-L 1584 – 2665

The statistical parameters reveal significant differences between the samples, with S4 exhibiting the roughest, most developed surface texture and the highest degree of anisotropy and irregularity. S1, on the other hand, has the smoothest and most uniform surface.

5. CONCLUSION

This study analyzed the influence of ultrafast laser ablation on the surface topography of Monel® alloy 400. The Abbott–Firestone curves revealed significant differences in material distribution, with Sample S4 showing the most developed surface profile, indicating a rougher texture, while S1 had the smoothest profile. The texture directions indicated distinct anisotropies across the samples, with S1 having a nearly isotropic texture, and S4 displaying more complex directional variations.

The statistical surface parameters highlighted substantial variation in roughness and functional behavior. Sample S4 exhibited the highest roughness values (Sq, Sa), steep gradients (Sdq), and developed interfacial area (Sdr), indicating its suitability for applications involving high friction and load–bearing capacities. In contrast, S1, with its lower roughness and smoother texture, may be more appropriate for applications requiring minimal surface irregularity.

Additionally, the material and void volume parameters revealed significant differences in the load–bearing capacity and fluid retention properties of the samples, with S4 showing a higher void volume and material capacity. Overall, the integration of these parameters provides a detailed understanding of the surface topography and potential functional applications of each sample.

References

[1] K. Ronoh, J. Novotný, L. Mrňa, A. Knápek, D. Sobola. Analysis of processing efficiency, surface, and bulk chemistry, and nanomechanical properties of the Monel® alloy 400 after ultrashort pulsed laser ablation, Mater Res Express, 11(1): 016514, 2024

[2] Z. Ahmad. Selection of materials for corrosive environment, in Principles of Corrosion Engineering and Corrosion Control, vol. 56, no. 1–2, Elsevier, 2006, pp. 479–549

[3] Special Metals, "MONEL® alloy 400." Accessed: Nov. 19, 2023. [Online]. Available: https://www.specialmetals.com/documents/technical–bulletins/monel–alloy–400.pdf.

[4] Y. Zhu, J. Wang, H. Liu, P. Ren, F. Yan. The tribocorrosion behavior of Monel 400 alloy in seawater at different temperatures, Tribol Int, 189: 108975, 2023

[5] Y. Zhu, J. Wang, H. Liu, P. Ren, F. Yan. Effect of Dissolved Oxygen Content on Tribo–Corrosion Behavior of Monel 400 Alloy in Seawater, Metals (Basel), 14(1): 6, 2023

[6] "Monel® Alloy 400." Accessed: Sep. 28, 2024. [Online]. Available: https://megamex.com/monel–400/

[7] K. Ronoh, J. Novotný, L. Mrňa, A. Knápek, D. Sobola. Effects of laser and scanning parameters on surface modification of MONEL® alloy 400 by picosecond laser, Opt Laser Technol, 172: 110514, 2024

[8] R. Boris, S. Petronić, K. Čolić, Z. Stević, A. Petrović, Ž. Mišković, D. Milovanović. Laser Processing of Ni–Based Superalloy Surfaces Susceptible to Stress Concentration, Metals (Basel), 11(5): 750, 2021

[9] R. Iris, F. Adjei–Kyeremeh, U. Vroomen, E. Westhoff, S. Bremen, A. Hohoi, A. Bührig–Polaczek. Qualification of a Ni–Cu Alloy for the Laser Powder Bed Fusion Process (LPBF): Its Microstructure and Mechanical Properties, Applied Sciences, 10(10): 3401, 2020

[10] M. Kukliński, A. Bartkowska, D. Przestacki. Microstructure and selected properties of Monel 400 alloy after laser heat treatment and laser boriding using diode laser, International Journal of Advanced Manufacturing Technology, 98(9–12): 3005–3017, 2018

[11] M. Kukliński, A. Bartkowska, D. Przestacki, G. Kinal. Influence of microstructure and chemical composition on microhardness and wear properties of laser borided Monel 400, Materials, 13(24): 1–15, 2020

[12] R.I. Merino, M.A. Laguna–Bercero, R. Lahoz, Á. Larrea, P.B. Oliete, A. Orera, J.I. Peña, M.L. Sanjuán, D. Sola. Laser processing of ceramic materials for electrochemical and high temperature energy applications, Boletín de la Sociedad Española de Cerámica y Vidrio, 61: S19–S39, 2022

[13] K. Ronoh, J. Novotný, L. Mrňa, A. Knápek, D. Sobola. Surface Structuring of the CP Titanium by Ultrafast Laser Pulses, Applied Sciences, 14(8): 3164, 2024

[14] L. Leggio, Y. Di Maio, A. Pascale–Hamri, G. Egaud, S. Reynaud, X. Sedao, C.L. Mauclair. Ultrafast Laser Patterning of Metals Commonly Used in Medical Industry: Surface Roughness Control with Energy Gradient Pulse Sequences, Micromachines (Basel), 14(2): 251, 2023

[15] K. Ronoh, D. Sobola, L. Mrňa, J. Novotný, R. Dallaev, A. Knápek, V. Kolařík, V. Holcman. Characterization of the picosecond laser–ablated HOPG using Raman spectroscopy and SEM microscopy, Mater Today Commun, 34: 105181, 2023

[16] S. Arulvel, D. Dsilva Winfred Rufuss, J. Akshat, K. Jayakrishna, S. Mridul. Laser processing techniques for surface property enhancement: Focus on material advancement, Surfaces and Interfaces, 42: 103293, 2023. doi: 10.1016/j.surfin.2023.103293.

[17] Ş. Ţălu, K. Ronoh, D. Sobola. The laser treatment's impact on the surface topography of MONEL® Alloy 400, used in the manufacturing of marine equipment components, Magazine of Hydraulics, Pneumatics, Tribology, Ecology, Sensorics, Mechatronics (HIDRAULICA), 2: 15–26, 2024.

[18] Ş. Ţălu. Micro and nanoscale characterization of three dimensional surfaces. Basics and applications. Napoca Star Publishing House, Cluj–Napoca, Romania, 2015.

[19] Ş. Ţălu, S. Stach, D. Raoufi, F. Hosseinpanahi. Film thickness effect on fractality of tin–doped In_2O_3 thin films. Electron. Mater. Lett. 11: 749–757, 2015

[20] Ş. Ţălu, N. Patra, M. Salerno. Micromorphological characterization of polymer–oxide nanocomposite coatings by atomic force microscopy and fractal geometry analysis, Prog. Org. Coat. 89: 50–56, 2015

[21] L. Dejam, S. Solaymani, A. Achour, S. Stach, Ş. Ţălu, N. Beryani Nezafat, V. Dalouji, A.A. Shokri, A. Ghaderi. Correlation between surface topography, optical band gaps and crystalline properties of engineered AZO and CAZO thin films, Chem. Phys. Lett., 719: 78–90, 2019
[22] Ş. Ţălu, R.P. Yadav, A.K. Mittal, A. Arman, C. Luna, A. Achour, M. Mardani, A. Ahmadpourian, S. Naderi, A.A. Zavarian, F. Hafezi, A. Saghi, A. Méndez, G. Trejo. Application of Mie Theory and fractal models to determine the optical and surface roughness of Ag–Cu thin films, Opt. Quantum Electron., 49: 256, 2917
[23] L. Dejam, S. Kulesza, J. Sabbaghzadeh, A. Ghaderi, S. Solaymani, Ş. Ţălu, M. Bramowicz, M. Amouamouha, A.H. Salehi Shayegan, A.H. Sari. ZnO, Cu–doped ZnO, Al–doped ZnO and Cu–Al doped ZnO thin films: Advanced micro–morphology, crystalline structures and optical properties, Results Phys. 44: 106209, 2023
[24] Ş. Ţălu, M. Bramowicz, S. Kulesza, A. Ghaderi, S. Solaymani, H. Savaloni, R. Babaee, Micromorphology analysis of specific 3–D surface texture of silver chiral nanoflower sculptured structures, J. Ind. Eng. Chem., 43: 164–169, 2016
[25] T. Hoseinzadeh, S. Solaymani, S. Kulesza, A. Achour, Z. Ghorannevis, Ş. Ţălu, M. Bramowicz, M. Ghoranneviss, S. Rezaee, A. Boochani, N. Maozaffari. Microstructures, fractal geometry and dye–sensitized solar cells performance of CdS/TiO_2 nanostructures, J. Electroanal. Chem., 830–831: 80–87, 2018
[26] Ş. Ţălu, P. Nikola, D. Sobola, A. Achour, S. Solaymani. Micromorphology investigation of GaAs solar cells: case study on statistical surface roughness parameters, J. Mater. Sci. Mater. Electron., 28: 15370–15379, 2017
[27] S. Solaymani, S. Kulesza, Ş. Ţălu, M. Bramowicz, N.B. Nezafat, V. Dalouji, S. Rezaee, H. Karami, M. Malekzadeh, E.S. Dorbidi. The effect of different laser irradiation on rugometric and microtopographic features in zirconia ceramics: study of surface statistical metrics, J. Alloys Compd., 765: 180–185, 2018
[28] C. Larosa, Ş. Ţălu, A.P. Reverberi, M. Salerno. Microporous morphology of cathodic electrolytic treated aluminum imaged by atomic force microscopy. Materials Letters, 280, 128593, 1–5, 2020
[29] D. Elenkova, J. Zaharieva, M. Getsova, I. Manolov, M. Milanova, S. Stach, Ş. Ţălu, Morphology and Optical Properties of SiO_2–Based Composite Thin Films with Immobilized Terbium(III) Complex with a Biscoumarin Derivative, Int. J. Polym. Anal. Charact. 20: 42–56, 2015
[30] Ş. Ţălu, S. Abdolghaderi, E.P. Pinto, R.S. Matos, M. Salerno, Advanced fractal analysis of nanoscale topography of Ag/DLC composite synthesized by RF–PECVD, Surf Eng., 2020
[31] S. Mohammad, A. Zelati, S. Rezaee, C. Luna, R.S. Matos, M.A. Pires, N.S. Ferreira, H.D. da Fonseca Filho, A. Ahmadpourian, Ş. Ţălu. Evaluating the Topological Surface Properties of Cu/Cr Thin Films Using 3D Atomic Force Microscopy Topographical Maps, Coatings, 12: 1364, 2022
[32] Ţălu, Ştefan, Sebastian Stach, Joana Zaharieva, Maria Milanova, Dimitar Todorovsky, and Stefano Giovanzana. Surface roughness characterization of poly(methylmethacrylate) films with immobilized Eu(III) β–Diketonates by fractal analysis. International Journal of Polymer Analysis and Characterization, vol. 19, no. 5 (2014): 404–421
[33] ISO 25178–2: 2012, Geometrical product specifications (GPS) – Surface texture: Areal – Part 2: Terms, definitions and surface texture parameters. Available from: http://www.iso.org (last accessed October 1st, 2024).
[34] Mountains Map® 10 Software (Digital Surf, Besançon, France). Available from: http://www.digitalsurf.fr (last accessed October 1st, 2024).

ISSN 1584 – 2665 (printed version); ISSN 2601 – 2332 (online); ISSN-L 1584 – 2665